



Unveiling enhanced dark photocatalysis: Electron storage-enabled hydrogen production in polymeric carbon nitride

Laiyu Luo^a, Siyu Wang^a, Liping Zhang^{b,*}, Xudong Xiao^a, Baogang Wu^a, Mietek Jaroniec^{c,*}, Baojiang Jiang^{a,*}

^a Key Laboratory of Functional Inorganic Material Chemistry, Ministry of Education of the People's Republic of China, Heilongjiang University, Harbin 150080, China

^b Faculty of Materials Science, Shenzhen MSU-BIT University, Shenzhen 518172, China

^c Department of Chemistry and Biochemistry, Kent State University, Kent, OH 44242, USA

ARTICLE INFO

Keywords:

Dark photocatalysis
Carbon nitride
Electron storage
Hydrogen evolution

ABSTRACT

Researchers have successfully replicated light-driven reactions of natural photosynthesis on semiconductors. However, an important problem limiting practical applications of these reactions is their dependence on light. Catalytic activity of the semiconductors is lost once light ceases, as the generation of charge carriers (i.e., electron-hole pairs) stops. In light of this problem, photosynthetic reactions in the dark are worthy of extra attention. Despite several reports on dark photocatalysis, the energy conversion efficiency remains low, and the mechanism is unclear. In this study, we developed an artificial photocatalytic system capable of decoupling the light and dark hydrogen production reactions. The system is composed of polymeric carbon nitride (PCN), in which electron storage sites are deliberately created. By tuning the number of the electron storage sites in the system, a record hydrogen production rate of $1480 \mu\text{mol g}^{-1} \text{h}^{-1}$ was achieved after termination of the visible-light ($\lambda > 420 \text{ nm}$) illumination. *In-situ* spectroscopic techniques reveal that these electron reservoirs are composed of cyanamide groups capable of storing electrons. Moreover, these electron reservoirs can be excited and show surface plasmon resonance (SPR) effects, leading to the enhanced optical absorption. Importantly, the oxidation side of the dark photocatalytic reaction is found to stem from a cascade reaction involving hole-derived radicals rather than electron-generated oxygenic species reported in literature. We established a complete and stepwise dark photocatalytic reaction process as well as distinguished a rate-determining step.

1. Introduction

Natural photosynthesis, including the light-dependent reactions in Photosystem I (PSI) and Photosystem II (PSII) and the light-independent reactions known as the Calvin cycle, is an efficient biochemical process that converts solar energy into energy-rich carbohydrates (Scheme 1a) [1]. By imitating the light-driven reactions of natural photosynthesis, researchers have developed artificial photocatalytic systems that can use solar energy to generate active species for various purposes, including water splitting, CO_2 reduction, and pollutant degradation, addressing many of the current energy and environmental challenges (Scheme 1b) [2]. However, artificial photocatalytic materials generally require continuous input of light to carry out the redox reaction, and they lack the ability to store electrons in the dark for further reactions as in natural photocatalytic systems, which limits their application [3–6]. Therefore, exploration of photocatalytic reactions in the dark is likely to create

additional value to this technology (Scheme 1c) [7–11]. So far, reports on the photocatalysts operating in the dark are limited. More importantly, the mechanism remains unclear and the energy conversion efficiency is low.

Recently, engineering the crystalline structure of PCN using molten salts has been developed as an effective strategy to enhance the photocatalytic activity [12–14]. On the one hand, an improvement in the crystallinity benefits the transfer of electrons and holes; on the other hand, molten salt treated PCN has shown interesting electron storage capacity and was found to have catalytic ability under dark conditions [3,15]. Specifically, photogenerated electrons can temporarily stay at the cyanamide sites created by molten salt treatment. These cyanamide sites resemble electron reservoirs and they lead to longer lifetimes of the charge carriers. They can be selectively released in the absence of light to produce hydrogen or other substances. Importantly, these free electrons under light irradiation experience resonant oscillations similar to

* Corresponding authors.

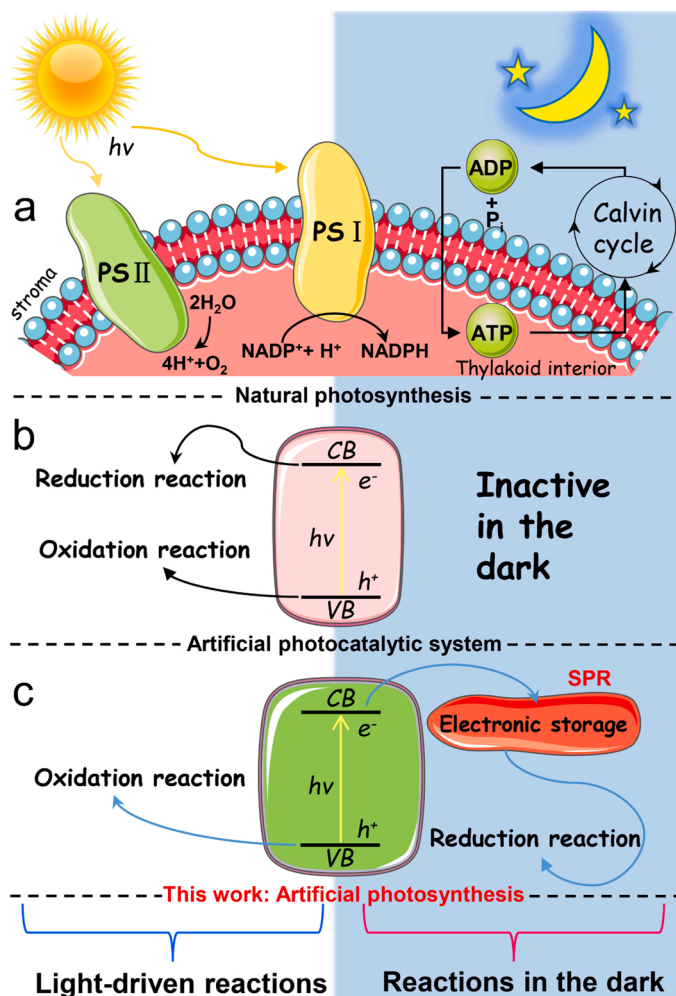
E-mail addresses: zhanglp@smbu.edu.cn (L. Zhang), jaroniec@kent.edu (M. Jaroniec), jbj@hlju.edu.cn (B. Jiang).

<https://doi.org/10.1016/j.apcatb.2023.123475>

Received 31 August 2023; Received in revised form 22 October 2023; Accepted 5 November 2023

Available online 7 November 2023

0926-3373/© 2023 Elsevier B.V. All rights reserved.



Scheme 1. Light-dependent process and light-independent process (in blue) of (a) a natural photosynthetic system, (b) a typical photocatalytic system, and (c) a photocatalytic system mimicking the natural photosynthetic system.

surface plasmon resonances (SPRs) observed in metal nanoparticles [16–18]. As a result, PCN with the cyanamide group shows significant optical absorption even in the near-infrared region, which is far beyond the absorption edge. However, the slow hydrogen production rate is far from practical usage. Apparently, the electron storage ability of PCN and the strength of the SPR effect scale with the concentration of the cyanamide group. However, it has been shown that excessive cyanamide groups hinder the transfer of the charge carriers, resulting in sluggish catalytic reactions. Therefore, it is of great importance to explore an appropriate concentration of the cyanamide group on PCN, at which optimal charge transfer and good electron storage are both ensured. In addition, the mechanism of reactions in the dark at the electron storage sites is not yet understood.

In this study, we show the synthesis of PCN with different degrees of crystallinity and concentrations of the electron storage sites in molten salts and at various temperatures. A supramolecular assembly was utilized as the precursor of PCN to produce hierarchical porous structures. It turned out that the chemical composition, optical absorption, and charge dynamics of these PCN materials all are significantly influenced by the calcining temperature. All the PCN materials synthesized in molten salts showed catalytic activity in the dark. Particularly, PCN synthesized at 500°C achieved a record hydrogen production rate of $1480\ \mu\text{mol g}^{-1}\text{ h}^{-1}$. In comparison, PCN prepared without using a molten salt did not produce any hydrogen in the dark. To understand the mechanism of the dark photocatalytic reactions, *in-situ* electron

paramagnetic resonance spectroscopy in the presence of various sacrificial agents were carried out to identify the active species involved. As a result, we established a complete and stepwise dark photocatalytic reaction process as well as distinguished a rate-determining step.

2. Experimental section

2.1. Synthesis of the supramolecular precursor and tubular carbon nitride (TCN)

The supramolecular precursor of carbon nitride was prepared according to the procedure in our previous report [61]. Briefly, 1 g of melamine and 1.2 g of phosphorous acid were added into 100 mL of deionized water. The mixture was stirred for 30 min and then transferred to an autoclave with a Teflon liner and heated at 180°C for 10 h, resulting in the precursor. Tubular carbon nitride was synthesized by heating the supramolecular precursor to 500°C for 4 h under a flow of nitrogen with a heating rate of 2.5°C/min .

2.2. Synthesis of CN-450-4, CN-500-4 and CN-550-4

Firstly, 1 g of TCN, 2.75 g of KCl and 2.25 g of LiCl were mixed and thoroughly ground. Next, the mixture was calcined in nitrogen in a tube furnace at $T^\circ\text{C}$ ($T = 450, 500, \text{ or } 550$) for t hours ($t = 2, 4, 6, \text{ or } 8$) with a heating rate of 2.5°C/min . The calcining solids were first soaked in deionized water for 24 h, and then collected by filtration and finally dried at 60°C for 8 h. The products were labeled as CN-T-t.

2.3. Synthesis of M500-4

M500-4 was prepared by following the synthetic procedure of CN-500-4 except that melamine was used as the precursor of carbon nitride.

2.4. In-situ PL spectroscopy

5 mg of a sample, 2.5 mL of water and 0.5 mL of benzyl alcohol were mixed and placed in a quartz cuvette. The mixture in the cuvette was bubbled with argon for 10 min and then sealed with a rubber stopper. The PL spectrum of the mixture was recorded immediately after it was irradiated by a 300-W xenon lamp equipped with an ultraviolet ($\lambda > 420\text{ nm}$) cut-off filter for 2 min.

2.5. UV-visible diffuse reflectance spectroscopy (DRS) of a sample in the blue state

5 mg of a sample, 200 μL of water and 100 μL of benzyl alcohol were mixed and the mixture was purged with argon for 10 min. The mixture was then placed between two coverslips. The DRS spectrum of the mixture was recorded immediately after it was irradiated with the 300-W xenon lamp equipped with an ultraviolet ($\lambda > 420\text{ nm}$) cut-off filter for 30 s.

2.6. Dark photocatalytic reaction of hydrogen production

The reactions were carried out on a PerfectLight Labsolar-6A all-glass automatic online trace gas analysis system. 5 mL of benzyl alcohol, 20 mg of a catalyst and 45 mL of water were mixed to prepare the reaction system. The mixture was sonicated for 10 min and then stirred for another 10 min. Prior to the dark photocatalytic reactions, the mixture was evacuated to remove air dissolved in the water. The light source was a 300-W xenon lamp equipped with an ultraviolet ($\lambda > 420\text{ nm}$) cut-off filter. The temperature of the reaction system was kept constant at 25°C . After irradiating the system for 1 h, the light was stopped and 3 wt% Pt was added. Next, the hydrogen production rate was recorded hourly. Gaseous products of the reactions were analyzed using an inline gas chromatograph (SP9700, TCD, molecular sieve 5 \AA , N_2 carrier, Beijing

Keruida Limited).

3. Results and discussion

Under light illumination, electron-hole pairs can be created in semiconductor photocatalysts. Cyanamide is an electron-accepting group that decelerates the relaxation of electrons to the ground state (Fig. 1a). However, excessive cyanamide groups on a photocatalyst reduces its crystallinity and increases the rate of electron-hole recombination. By using time-dependent density-functional theory (TD-DFT) and the structural models shown in Fig. S1, we studied the impact of different numbers of cyanamide on PCN on the charge separation efficiency. The charge density distribution diagram of the excited states reveals that electrons mostly distribute near the cyanide group, and holes near the heptazine ring. The presence of cyanamide groups in the

heptazine system leads to highly delocalized distributions of electrons and holes (Fig. 1 b, c, d, e, f), suggesting improved charge separation. We also calculated the average distances between the distributions of electrons and holes as well as the overlapping percentages for the heptazine systems (Fig. 1g) [19]. It turns out that the system with three cyanamide groups has the best separation of electrons and holes. The computational study indeed proves the existence of an optimal concentration of cyanamide groups on PCN that corresponds to a good balance between electron transfer/storage and charge recombination.

Studies have demonstrated that PCN prepared in the presence of molten salts has a larger degree of condensation due to improved diffusion of the reactant molecules as compared to that synthesized in the solid phase [20–22]. Importantly, the molten salts are also responsible for the formation of cyanamide groups [23,24]. The concentration of cyanamide groups in the PCN sample has been found to exhibit a

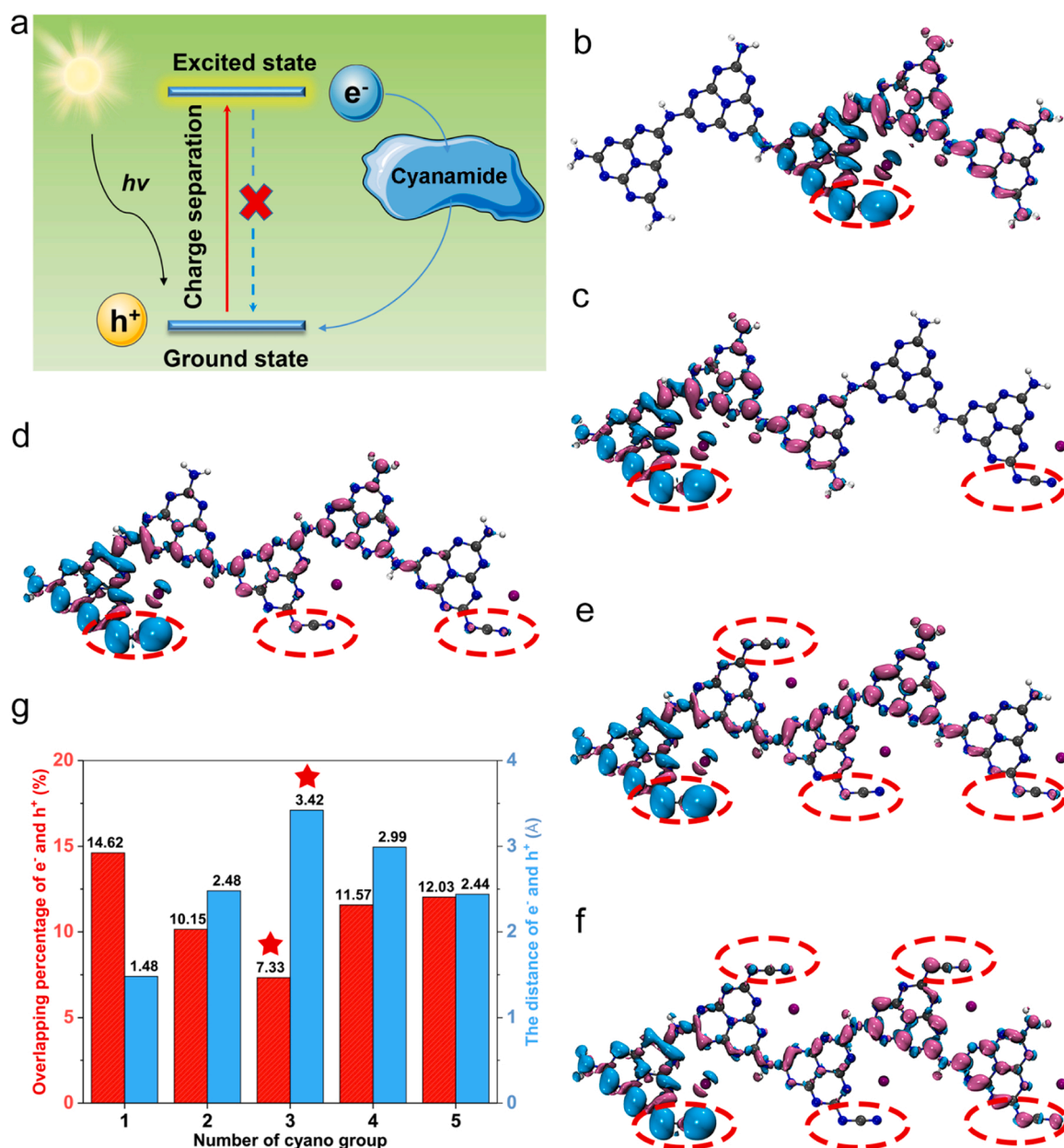


Fig. 1. (a) Schematic diagram of the process of electron transition, transfer, storage, and relaxation in PCN with cyanamide. Distributions of electrons and holes on five heptazine rings containing (b) one, (c) two, (d) three, (e) four and (f) five cyanamide groups (black, C; blue, N; gray, H; light purple, K; cyan, electron; dark purple, hole). (g) Percentage of overlap between the spatial distributions of electrons and holes and distance between the central points of the distributions as a function of the number of cyanamide groups on five heptazine rings.

correlation with the material's crystallinity [26]. This relationship can be assessed through various structural characterization techniques, including FTIR, XPS, and XRD. Therefore, it is expected that the crystallinity of PCN as well as its cyanamide content can be tailored by adjusting the calcination temperature. In preparation for polymeric carbon nitride (PCN), a supramolecular precursor was first heated at 500 °C in nitrogen for 2 h, creating carbon nitride with a tubular structure (labeled as TCN, Fig. 2a). Subsequently, TCN was mixed with KCl/LiCl and the mixture was calcined in nitrogen at T °C ($T = 450, 500$, or 550) for t hours ($t = 2, 4, 6$, or 8). It is noteworthy that the binary salt system, which has a melting point of ~ 355 °C, was added to provide a liquid environment for the precursor molecules [25]. This liquid environment is believed to favor the diffusion and the subsequent condensation processes of the precursor molecules and in turn lead to improved crystallinity of PCN as compared to the case of PCN synthesized in a solid phase [20]. The products after the calcination are named as CN- T - t , for instance CN-450-4, CN-500-4 and CN-550-4. Morphology of carbon nitride was studied using scanning electron microscopy (SEM, Fig. 2). Bulk carbon nitride synthesized by calcining melamine is composed of chunks of irregular structures (Fig. S2a,b). Heating the bulk carbon nitride in molten salts produced PCN (labeled as M500-4) made up of aggregates of needles (Fig. S2c), while calcination of TCN in the presence of the molten salts transformed the tubular structure into assemblies of particles (Fig. S3, Fig. 2b, c, d, and Fig. S4). For CN-450-4, the particles are loosely dispersed; as the calcination temperature was increased, the particles further aggregated, resulting in a highly dense structure. Elemental mappings show that CN- T - t is composed of C, N and K elements, which are uniformly distributed across the samples (Fig. 2e). Elemental analysis and inductively coupled plasma-atomic emission spectroscopy did not reveal any additional element (see Table S1 and Table S2). With rising calcination temperature, the C/N mass ratio

increases and approaches to the theoretical value for graphitic carbon nitride; in other words, the crystallinity is improved (Table S1).

Various techniques including Fourier transform infrared (FT-IR) spectroscopy, solid-state ^{13}C nuclear magnetic resonance (NMR) spectroscopy, electron paramagnetic resonance (EPR) spectroscopy, X-ray photoelectron spectroscopy (XPS), and X-ray absorption spectroscopy (XAS) were utilized to study the chemical structure of TCN and CN- T - t . FT-IR spectra of TCN and CN- T - t all show a group of peaks between 1100 and 1660 cm^{-1} (Fig. 3a), which have been attributed to the vibrations of sp^3 -type C-N bonds and sp^2 -type C=N bonds [26]. These atoms and bonds are building units of the aromatic rings, the bending vibration of which is evident from the peak at 810 cm^{-1} . Therefore, carbon nitride based on the heptazine ring systems was indeed synthesized by following the procedure in this work. Interestingly, the FT-IR spectra of CN- T - t also present two additional groups of peaks (highlighted in blue and yellow) that are absent in the spectrum of TCN. The peak at ~ 993 cm^{-1} (in the blue zone) is ascribed to the asymmetric vibration of the metal-NC₂ bond, while the two peaks at ~ 2178 cm^{-1} (in the purple zone) and ~ 3420 cm^{-1} (in the yellow zone) correspond to the cyanamide group and the terminal amino group of the heptazine ring, respectively [23]. Moreover, the area of these new peaks for CN- T - t decreases with increasing calcination temperature, indicating a decline in the proportion of these groups in the samples. Further, calcination for long times (>4 h) also leads to a decrease in the peak area (Fig. S8). In other words, the concentration of the cyanamide groups in carbon nitride can be adjusted by using molten salts in the synthesis and calcinating the precursor at different temperatures for different time periods.

The ^{13}C NMR spectrum of TCN exhibits two peaks (No. 2 and 3) at chemical shifts of 154 and 164 ppm (Fig. 3b), respectively, corresponding to two different types of C atoms in the heptazine rings [27,

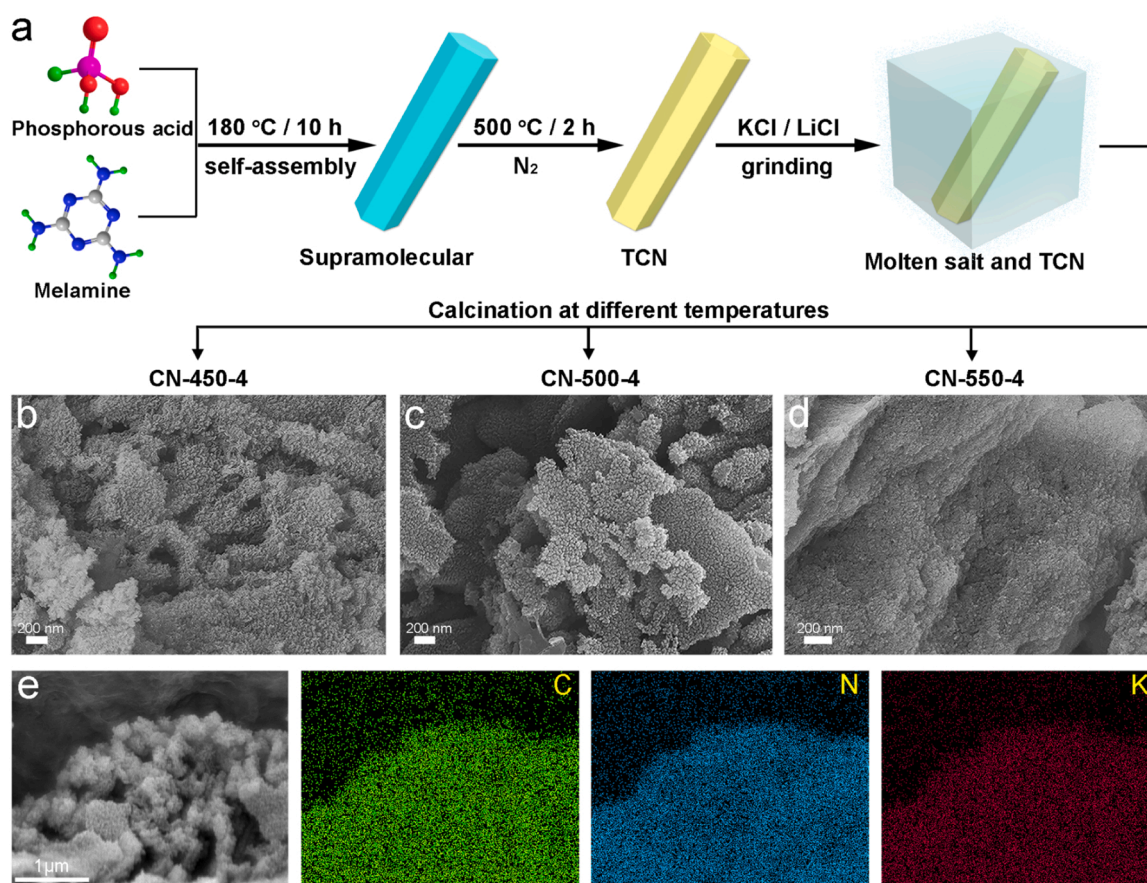


Fig. 2. (a) Synthetic route of a CN- T - t sample. (b-d) SEM images of CN-450-4, CN-500-4, CN-550-4. (e) Elemental mapping of CN-500-4.

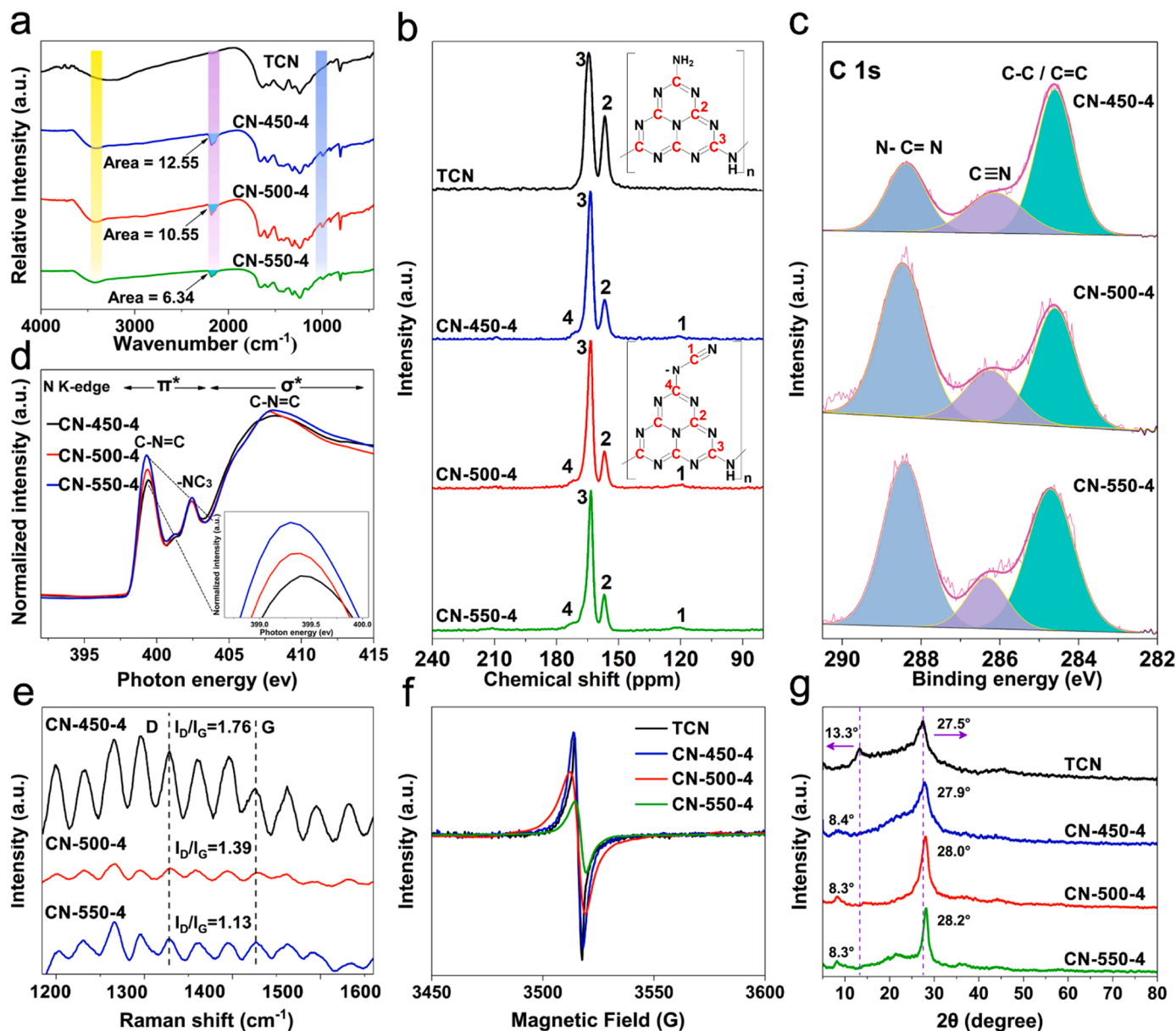


Fig. 3. (a) Normalized FT-IR spectra, (b) solid-state ^{13}C NMR spectra, (c) C 1 s XPS spectra, (d) N K-edge XANES spectra, (e) Raman spectra (785 nm excitation), (f) solid-state EPR spectra, and (g) normalized XRD patterns of TCN and CN-T-t.

28]. The presence of cyanamide groups in CN-T-t is further evidenced by additional peaks at 120 and 172 ppm (No. 1 and 4) in the NMR spectra. Peak No. 1 is assigned to C of the cyanamide group (labeled as C1), while peak No. 4 is attributed to C of heptazine that is nearest to the cyanamide group (labeled as C4).

Quantification of the cyanamide group in CN-T-t was carried out using XPS. The C1s XPS spectra of CN-T-t reveal three different chemical states of the C atoms (Fig. 3c), namely adventitious carbon (C-C/C=C, 284.6 eV), cyanamidedecarbon (C≡N, 286.1 eV) and carbon in the N-C=N aromatic ring (aromatic carbon, 288.4 eV) [26]. With increasing calcination temperature, the peak area of the cyanamidedecarbon decreases, while that of the aromatic carbon grows, which is expected as calcination at high temperatures favors the formation of the aromatic rings.

The N1s XPS spectra (Fig. S5) were deconvoluted to give three peaks at 398.6 eV, 400.4 eV and 401.6 eV, corresponding to the nitrogen atoms of C-N=C, N-C₃ and C-N-H, respectively [26]. As the calcination temperature rises, the area of the N-C₃ peak increases while that of the

C-N-H peak decreases, which is in line with the result of the C 1 s XPS spectra. Interestingly, calcination at a higher temperature caused the N-C₃ peaks to move toward larger binding energies. This shift was caused by the change in the electronic structure of N due to the formation of cyanamide groups, which give rise to a N1s XPS peak located between those for C-N=C and N-C₃ [26]. In addition, O 1 s XPS spectra showed a signal of the presence of adsorbed oxygen in the sample (Fig. S6).

Effects of calcination temperature on the heptazine ring systems of carbon nitride are additionally revealed in the XANES spectra. π^* resonances associated with the N-C=N (or C-N=C) bonds are seen to strengthen as the calcination temperature increases (Figs. S7 and 3d), which again indicates that elevated temperatures are conducive to the formation of carbon nitride with a large degree of condensation and an ordered in-plane structure [29,30].

Considering that the building unit of carbon nitride, i.e., heptazine, is a highly conjugated system, we studied the free electrons using room-temperature electron paramagnetic resonance (EPR) spectroscopy

(Fig. 3f). As expected, all the EPR spectra feature a peak at a g value of about 2.0034 due to the presence of unpaired electrons in the conjugated framework [31–33,58]. The presence of these electrons can be ascribed to defects originating from C or N atom vacancies, wherein the absence of a specific atom results in a surplus of electrons that are distributed amongst the adjacent atoms. These surplus electrons then proceed to delocalize within the π -conjugated network of the carbon nitride structure, thereby elevating the overall concentration of lone-pair electrons. The intensity of the EPR peak decreases with increasing calcination temperature and time (Fig. S8), which leads to higher degrees of polymerization of PCN.

X-ray diffraction (XRD) experiments confirm that all the products possess two types of long-range order (Fig. 3g), which is in line with the structure of PCN. In addition, the XRD patterns of CN- T - t show more intense peaks than that of TCN does, corroborating the ability of the molten salts to improve the crystallinity of carbon nitride. Interestingly, the (100) peaks at 13° corresponding to in-plane structural ordering for CN- T - t are shifted to smaller diffraction angles as compared to that for TCN, while their (002) peaks at 27° due to the layered structure are located at larger diffraction angles. With increasing calcination

temperature and time, the magnitude of the shift grows (Fig. S8). The peak shifts confirm that the molten salts leads to a decrease in the distance between adjacent carbon nitride layers while an increase in the spacing of the in-plane building units. Moreover, the observed peak shifts indicate a structural transition from a melon-type configuration to a poly(heptazine imide)-type (PHI-type) configuration, which is associated with an increase in the crystallinity. The influence of calcination temperature on the structural ordering of powder PCN is also evident from the Raman spectra (Fig. 3e). The broad and asymmetric peaks observed in the range of $1200 - 1700 \text{ cm}^{-1}$ can be attributed to the stretching vibrations of the C-N bonds [59]. Specifically, two distinct peaks were observed at 1321 cm^{-1} (referred to as the D band) and 1561 cm^{-1} (referred to as the G band). The G band is attributed to graphite-like sp^2 microdomains in the samples, while the D band corresponds to disordered sp^2 microdomains introduced by the linking with N atoms [59]. As can be seen, the ratio of the D band intensity to the G band intensity (I_D/I_G), accordingly the concentration of defects in PCN, decreases with declining calcination temperature; in other words, calcination of the precursor of PCN at higher temperatures results in more ordered structures. In addition, the peaks at 997 cm^{-1} for

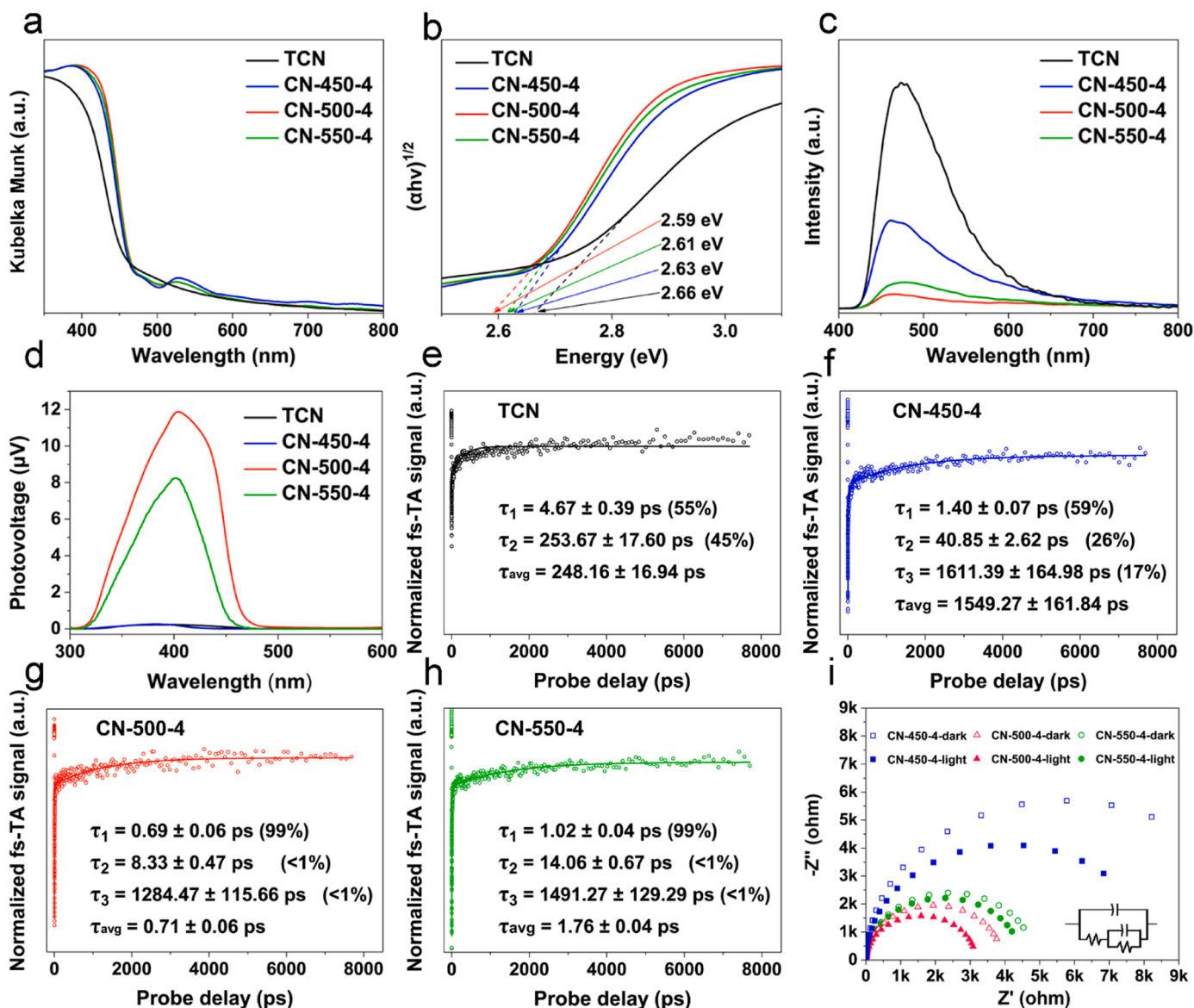


Fig. 4. (a) UV-Vis diffuse reflectance spectra, (b) tauc plots, (c) steady-state photoluminescence spectra, (d) surface photovoltage spectra, (e-h) transient absorption spectroscopy and (i) Nyquist plots of TCN and CN- T - t .

CN-500-4 and CN-550-4 are weakened. The Raman peaks at 997 cm^{-1} correspond to the symmetric N-breathing mode of heptazine units. The specific surface area (SSA) of M500-4 and CN-*T-t* was determined from nitrogen adsorption-desorption isotherms using the Brunauer-Emmett-Teller (BET) model (Figs. S9 and S10). SSA of M500-4 is about $34\text{ m}^2\text{ g}^{-1}$, while CN-450-4, CN-500-4 and CN-550-4 have larger specific surface areas of 43, 66, $57\text{ m}^2\text{ g}^{-1}$, respectively, indicating the advantage of the supramolecular precursor of carbon nitride [34].

Optical absorption ability of powdery TCN and CN-*T-t* samples was studied by conducting UV-visible diffuse reflectance spectroscopy. Absorption edges (λ_{edge}) of all the CN-*T-t* products are located at longer wavelengths than that of TCN is. λ_{edge} of CN-450-4 is close to λ_{edge} of CN-550-4, but it is smaller than that of CN-500-4 (Fig. 4a). From the Tauc plots, the band gaps (E_g) of TCN, CN-450-4, CN-500-4, and CN-550-4 are calculated to be 2.66 eV, 2.63 eV, 2.59 eV and 2.61 eV, respectively (Fig. 4b). Interestingly, a new absorption peak appears in the spectra of CN-*T-t* at around 550 nm, which has been ascribed to the $n \rightarrow \pi^*$ electron transition [35–37]. This transition is forbidden for the s-triazine or heptazine structure with a planar symmetry but becomes allowed after the symmetry is broken. In this case, the disruption of the melon structure during the molten salt treatment serves as a potential mechanism for breaking the symmetry and enabling this transition. Position of the bottom of the conduction band (E_{cb}) of CN-*T-t* was assessed electrochemically from Mott-Schottky plots at different frequencies (Fig. S11). By combining E_{cb} and E_g , we can determine the edge of the valence band (E_{vb}) of CN-*T-t* and in turn the band structure (Fig. S11d).

Charge dynamics of TCN and CN-*T-t* were explored by using photoluminescence (PL) spectroscopy. For TCN, photogenerated electrons and holes quickly recombine and cause strong photoluminescence as can be seen in the steady-state PL spectrum (Fig. 4c). However, after the formation of cyanamide groups the electron-hole recombination is greatly suppressed due to the electron storage ability of cyanamide [6]. Particularly, PL spectrum of CN-500-4 has the weakest fluorescence peak, indicating its best electron reservoir capacity despite CN-500-4 having a smaller number of cyanamide groups than CN-450-4. It is likely that the extra cyanamide groups become new recombination centers for electron-hole pairs. The electron storage ability of TCN and CN-*T-t* was verified by measuring change in the surface potential, namely surface photovoltage (SPV), as well as photocurrent under illumination of light at different wavelengths (Figs. 4d and S12). Indeed, SPV and the photocurrent of CN-500-4 are constantly larger than those of other carbon nitride materials studied since more electrons can be captured by the cyanamide groups.

Dynamical processes of CN-*T-t* were studied using ultrafast transient absorption (TA) spectroscopy. In our experiments, TCN and CN-*T-t* samples were excited by a femtosecond visible light pulse and probed by pulses with wavelengths in the range of 430–760 nm (Fig. S13). At 521 nm strong TA signals were recorded, and the spectra were fitted using the exponential decay function, resulting in two time constants (τ_1 and τ_2) for TCN and three time constants (τ_1 , τ_2 and τ_3) for CN-*T-t* (Fig. 4e–h). $\tau_1 = 4.67\text{ ps}$ and $\tau_2 = 253.67\text{ ps}$ for TCN are ascribed to trapping and radiative recombination, respectively. The additional time constant (τ_1) for CN-*T-t* is attributable to the relaxation of hot electrons, which typically have a lifetime on the order of 1 ps [38]. In CN-450-4, radiative recombination contributes appreciably to the decay process likely because of an excess of the cyanamide groups acting as the recombination centers, which is in line with the PL result. In comparison, the electron-hole annihilation is significantly reduced in CN-500-4 and CN-550-4, while relaxation of hot electrons dominates the decay. Electrochemical impedance spectroscopy (EIS) provides valuable insights into the migration efficiency of photogenerated carriers [60]. As depicted in Fig. 4i, CN-500-4 exhibits a smaller semicircle in the Nyquist plot than CN-450-4 and CN-550-4, suggesting a larger

efficiency of carrier separation and a lower charge transfer resistance in CN-500-4. Interestingly, the semicircle became smaller after light exposure of CN-500-4 likely due to its ability to store electrons.

In-situ EPR spectra of CN-*T-t* after two minutes of light exposure indicate that the electron-storage ability of the products decreases in the order CN-500-4 > CN-550-4 > CN-450-4 (Fig. 5a). *In-situ* PL spectra are used to evaluate the electron-hole recombination in CN-*T-t* (Fig. 5b), and they show a significant decrease in the intensity of fluorescence after illumination, which is due to the synergetic effect of the storage of electrons and suppression of charge recombination. In particular, the *in-situ* PL spectrum of CN-500-4 possesses the smallest fluorescence intensity owing to its best electron-storage ability. Interestingly, the color of CN-500-4 and CN-550-4 changed from yellow to blue after they were irradiated by light due to the accumulation of significant numbers of electrons (insets of Figs. 5a and 5b).

Since electron storage in CN-*T-t* resembles the charging process of a pseudocapacitor, quantification of the electron storage ability of CN-*T-t* can be achieved using photoelectrochemical methods, including galvanostatic charge-discharge (GCD) cycling and cyclic voltammetry (CV). The measurements were performed using 0.1 mol/L Na_2SO_4 containing an appropriate amount (1 vol%) of benzyl alcohol as the electrolyte. Prior to measurements, the electrolyte was bubbled with argon to remove dissolved oxygen. The GCD curve of CN-500-4 reveals a discharge duration of up to 130 s at a current density of 1 A/g (Fig. 5c); the specific capacitance was determined to be 21.68 F g^{-1} (Fig. S14). Fig. 5d shows the CV curves of CN-*T-t* at a scan rate of 100 mV s^{-1} . Clearly, the CV curve of CN-500-4 encloses an area larger than the other products do, which means that CN-500-4 has the largest specific capacitance (Fig. S15). Again, the result of the electrochemical measurements resonates that of the spectroscopic approaches. Furthermore, we conducted GCD tests on the cyanamide-free TCN samples; however, an electron storage behavior as shown in the CN-*T-t* samples was not observed. Therefore, the cyanamide group can function as an electron acceptor. Based on the experimental and theoretical results, it can be reasoned that an excessive amount of the cyanamide group (as in CN-450-4) leads to decreased crystallinity and an increase in the rate of electron-hole recombination. Conversely, insufficient cyanamide groups (as in CN-550-4) are not favorable for effective electron storage. Furthermore, the UV-visible diffuse reflectance spectra of CN-500-4 before and after light illumination (i.e., blue CN-500-4) in the presence of benzyl alcohol were recorded (Fig. 5e). It turned out that blue CN-500-4 possesses strong optical absorption even beyond the absorption edge. This phenomenon resembles that observed in the absorption spectra of metal nanoparticles and it can be attributed to SPRs due to the accumulation of photogenerated electrons [16,17]. The spectra of CN-450-4 and CN-550-4 also show enhanced absorption at larger wavelengths; nevertheless, the magnitudes of enhancement are smaller than that for CN-500-4 (Fig. S16). Carbon nitride is known to be an n-type semiconductor and therefore the potential of CN-500-4's conduction band bottom (V_{cb}) is approximated as the flat-band potential (V_{F}). CN-500-4 in the yellow and blue states has different flat-band potentials of -0.7 V and -1.26 V , respectively, against the normal hydrogen electrode (NHE, Fig. 5f). The more negative V_{F} (i.e., V_{cb}) of the blue-state CN-500-4 additionally suggests the occurrence of electron accumulation after light irradiation.

Owing to the excellent optical absorption and electron storage ability of CN-*T-t*, these samples were used for dark photocatalytic hydrogen production reaction. In the presence of benzyl alcohol, CN-500-4 exhibited a normalized hydrogen production rate of $1480\text{ }\mu\text{mol g}^{-1}\text{ h}^{-1}$ within the first hour after the lamp was turned off, whereas TCN did not produce any hydrogen (Fig. 6a). Performance stability tests were conducted on CN-500-4, and the photocatalytic performance exhibited 69.9 % retention of the initial run at the sixth run (Fig. S17). Additionally, benzyl alcohol was completely converted to benzaldehyde with high selectivity (Fig. S18). Fig. 6b shows the dark photocatalytic hydrogen production performance of various reported catalysts under similar

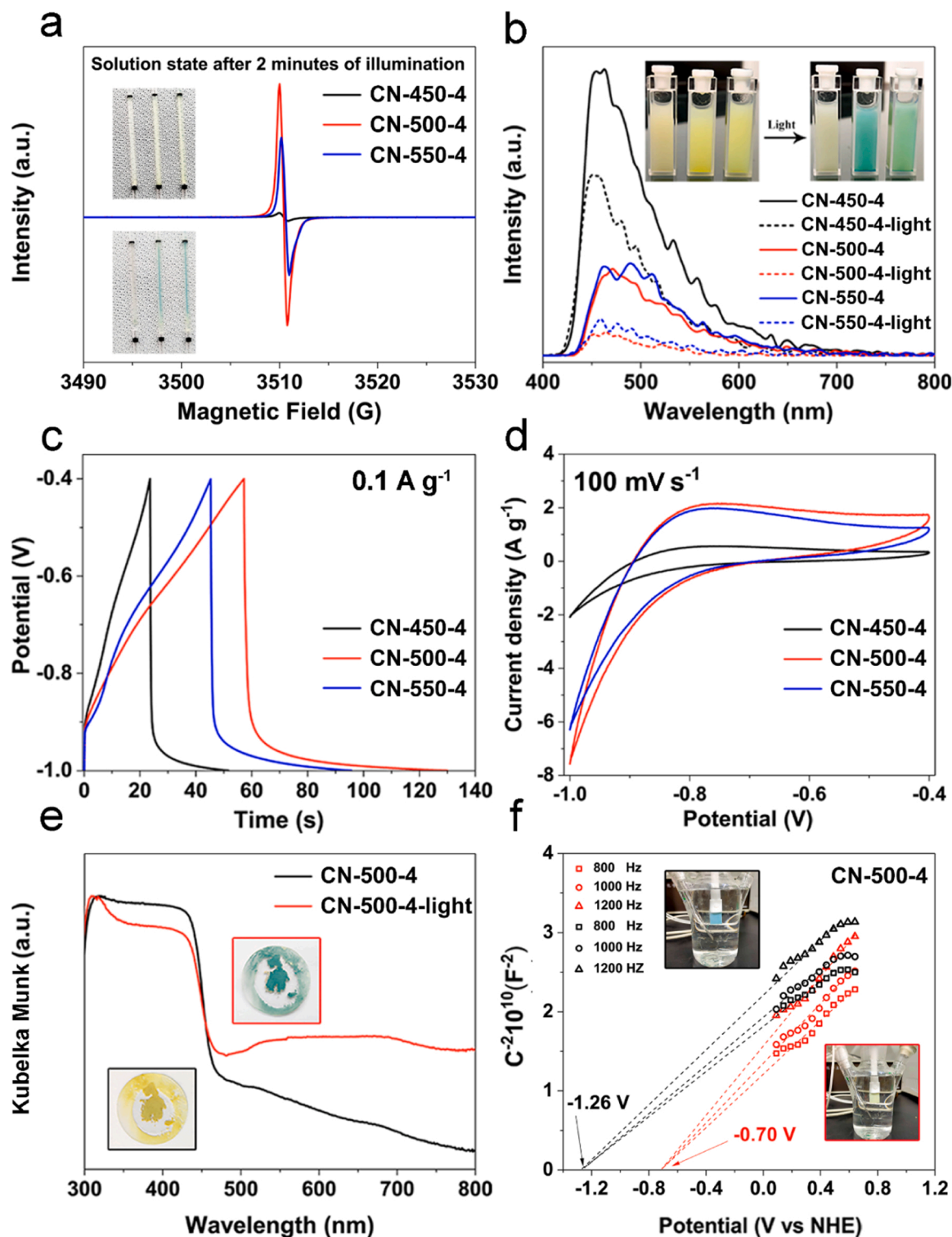


Fig. 5. (a) *In-situ* EPR spectra of CN-*T-t* in a mixture of H₂O and benzyl alcohol, (b) *In-situ* PL spectra of CN-*T-t* in the mixture before and after illumination, (c) GCD and (d) CV curves of CN-*T-t* recorded at 0.1 A g⁻¹ and 100 mV s⁻¹, respectively, (e) *In-situ* diffuse reflectance spectra of a mixture of water, benzyl alcohol and CN-500-4 before and after illumination. (f) Mott-Schottky plots of CN-500-4 in an electrolyte with (black border) or without (red border) benzyl alcohol.

conditions. As can be seen, CN-500-4 of this work achieved the highest hydrogen production rate, which is attributable to the construction of electron storage sites and enhanced SPR effect. During the dark photocatalytic reaction with CN-500-4, the catalyst changed color from yellow to blue and then back to yellow (Fig. S19). The first color change originated from the accumulation of electrons in the cyanide-modified framework, while the second color change was caused by the addition

of chloroplatinic acid, which was reduced to platinum metal, improving electron transport [3,6,39]. In contrast, no color change was observed for cyanamide-free TCN sample. (Fig. S20) Accumulation of the electrons led to high-energy electron reservoirs as indicated by the more negative flat-band potential, and the release of the electrons was responsible for hydrogen production in the dark.

To explore a suitable photocatalyst-water-alcohol system,

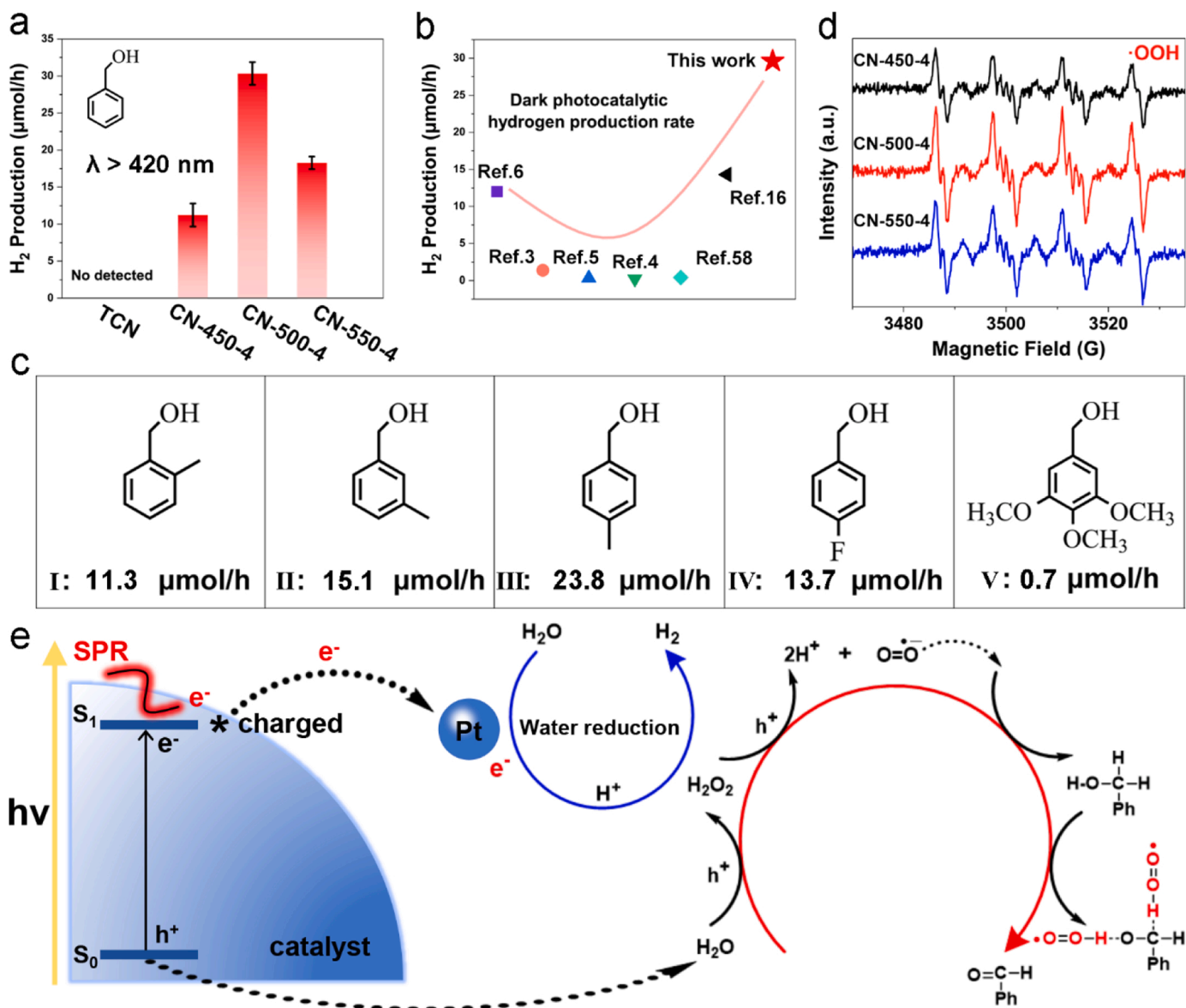


Fig. 6. (a) Dark photocatalytic hydrogen production rates of TCN and CN-T-t in a benzyl alcohol-water mixture after the cessation of visible-light ($\lambda > 420$ nm) illumination. (b) Hydrogen production rates of catalysts in dark photocatalytic reactions. (c) EPR spectra of mixtures of CN-T-t, DMPO, H_2O and benzyl alcohol after light illumination. (d) Different rates of hydrogen production in the presence of various alcohols. (e) Proposed mechanism of hydrogen evolution coupled with benzyl alcohol oxidation.

photocatalytic hydrogen production in the presence of different alcohols was carried out (Fig. 6c). In addition to the changes caused by different substitution positions, the effects of different substituent species were also examined, which also showed different rates of hydrogen production. The alcohols examined include three isomers of methylbenzyl alcohol (I, II, and III of Figs. 6c), 4-fluorobenzyl alcohol, and 3,4,5-trimethoxybenzyl alcohol in addition to benzyl alcohol. Interestingly, the position of methyl on the benzene ring is found to play a significant role in the hydrogen production (a, b, c in Fig. 6c). The use of 2-methylbenzyl alcohol resulted in a hydrogen production rate (11.3 $\mu\text{mol/h}$) smaller than that when 3-methylbenzyl alcohol (15.1 $\mu\text{mol/h}$) was used, which is in turn smaller than the rate in the case of 4-methylbenzyl alcohol (23.8 $\mu\text{mol/h}$). Additionally, the substitution of 4-fluorobenzyl alcohol for 4-methylbenzyl alcohol led to a decrease in the rate of hydrogen production to 13.7 $\mu\text{mol/h}$. The above changes can be explained by electron-donating and -withdrawing properties. The increase in different substitution positions and different substituents caused a change in the distribution of the electron cloud density, which led to a

change in the oxidation rate of the alcohol. It is reasoned that the position and identity of a group or element on the benzene ring affect the electron cloud around the hydroxyl group; replacement of methyl or change of the position on the benzene ring alters the oxidation rate of the alcohol, which further leads to differing reduction rates of hydrogen ions [40]. In addition, the methylbenzyl alcohols were less effective than benzyl alcohol, which is ascribed to the steric effect because it makes adsorption of the former alcohols on the photocatalyst more difficult [41]. After using 3,4,5-trimethoxybenzyl alcohol (V of Fig. 6c), strong steric hindrance from the methoxy group led to a hydrogen production rate of mere 0.7 $\mu\text{mol/h}$. A large steric hindrance would inhibit the adsorption of molecules on the catalyst surface and lead to a decrease in activity [41].

It has been reported that the rate of overall water splitting is limited by the oxidation of water [42]. In the absence of an alcohol, the evolution rates of hydrogen and hydrogen peroxide, which are the products of water reduction and oxidation, respectively, are low (Fig. S21). To understand the mechanism of the oxidation reaction, EPR experiments

involving the systems of CN-T-t, H₂O, benzyl alcohol and 5,5-dimethyl-1-pyrroline N-oxide (DMPO) after photoexcitation were conducted. In the previous reports [42], signals of carbon-centered radicals [$\bullet\text{CH}(\text{OH})\text{Ph}$] were detected and the radical was considered to be responsible for alcohol oxidation, while the EPR spectra in this work reveal an alternative mechanism based on $\bullet\text{OOH}$ (Fig. 6d) [43–46].

Four possible mechanisms of the oxidation of benzyl alcohol involving photogenerated electron-hole pairs and free radicals have been discussed in literature and examined in this work (Fig. S22) [47–58]. In the water splitting experiment, initially only hydrogen and H₂O₂ were detected. The signals of $\bullet\text{O}_2^-$ and carbon-centered free radicals are missing in the EPR spectrum, eliminating the possibility of reaction pathways a, b, and c in Fig. S22 being the responsible mechanism. In addition, pathway d can also be ruled out due to the failure in the detection of $\bullet\text{OH}$, which agrees with the fact that the valence band potential of PCN is too low to directly oxidize hydroxyl into $\bullet\text{OH}$.

A fifth mechanism for the coupled reaction of hydrogen evolution and benzyl alcohol oxidation is proposed (Fig. 6e). After photoexcitation of a carbon nitride photocatalyst, electron-hole pairs are generated. Electrons are first stored in the cyanamide group, and then transfer to Pt particles, which were formed on the photocatalyst from the photoreduction of chloroplatinic acid. Subsequently, electrons in Pt are captured by hydrogen ions, resulting in hydrogen molecules. It is worth noting that after acetonitrile was substituted for water in the photocatalytic experiments, hydrogen was hardly produced, confirming the role of water instead of the alcohol as the hydrogen source. The hole-triggered oxidation of the alcohols is a cascade reaction. First, holes oxidize water into H₂O₂ and then $\bullet\text{O}_2$. Next, two hydrogen atoms of benzyl alcohol combine with $\bullet\text{O}_2$. The subsequent release of $\bullet\text{OOH}$ radicals generates benzaldehyde. Notably, according to the results in Fig. 6c, the ease of alcohol oxidation, which affects the hydrogen production, indicates that alcohol oxidation at the oxidation end is a rate-limiting step.

4. Conclusions

In this work, we demonstrate polymeric carbon nitride (PCN)-based photocatalysts with high activities for hydrogen production in the dark. The excellent performance of the dark photocatalysts is rooted in their ability to function as electron reservoirs, which also leads to the improved light absorption due to SPRs. Various spectroscopic techniques revealed that the synthesis of carbon nitride in the presence of molten salts resulted in cyanamide groups, which can store photo-generated electrons. In particular, calcination at 500 °C for 4 h produced a PCN material (CN-500-4) with the most suitable number of cyanamide groups. In the dark, CN-500-4 gave a record hydrogen production rate of 1480 $\mu\text{mol g}^{-1} \text{h}^{-1}$, while no hydrogen was produced over PCN prepared without using a molten salt (TCN). Meanwhile, after 2 h of reaction nearly 100 % of benzyl alcohol was converted to benzaldehyde. A stepwise mechanism has been identified to be responsible for the dark photocatalytic hydrogen evolution. Additionally, oxidation of the alcohol is a cascade reaction that involves H₂O₂, $\bullet\text{O}_2$ and $\bullet\text{OOH}$ radicals. The creation and characterization of electron-storage groups on PCN as well as the ability of these groups to greatly improve hydrogen evolution is expected to be applicable to other photocatalysts and applications.

CRedit authorship contribution statement

Laiyu Luo: Investigation, Writing – original draft. **Siyu Wang:** Formal analysis, Software. **Xudong Xiao and Baogang Wu:** Investigation, Software, Data curation. **Liping Zhang and Mietek Jaroniec:** Supervision, Project administration. **Baojiang Jiang:** Supervision, Funding acquisition.

Declaration of Competing Interest

The authors declare that they have no known competing financial interests or personal relationships that could have appeared to influence the work reported in this paper.

Data availability

Data will be made available on request.

Acknowledgements

This work was supported by the National Natural Science Foundation of China (52273264, 12104209), Outstanding Youth Fund of Heilongjiang Province (JQ 2020B002).

Appendix A. Supporting information

Additional experimental details and data, including Structural models for TD-DFT, Synthetic route of a M500-4, SEM images, TEM images, N1s XPS spectra, C K-edge XANES spectra, FT-IR spectra, EPR spectra, XRD patterns, Brunauer-Emmett-Teller surface area, Mott-Schottky plots, Photocurrent responses, Specific capacitance, CV curves, UV/vis diffuse reflectance spectra, GC chromatogram and MS spectra, Photos of the reaction system, H₂O₂ yield, Possible mechanisms of alcohol oxidation. Supplementary data associated with this article can be found in the online version at [doi:10.1016/j.apcatb.2023.123475](https://doi.org/10.1016/j.apcatb.2023.123475).

References

- [1] J. Lv, J. Xie, A.G.A. Mohamed, X. Zhang, Y. Feng, L. Jiao, E. Zhou, D. Yuan, Y. Wang, Solar utilization beyond photosynthesis, *Nat. Rev. Chem.* 7 (2023) 91–105.
- [2] S. Cao, J. Low, J. Yu, M. Jaroniec, Polymeric photocatalysts based on graphitic carbon nitride, *Adv. Mater.* 27 (2015) 2150–2176.
- [3] V.W. Lau, D. Klose, H. Kasap, F. Podjaski, M.C. Pignie, E. Reisner, G. Jeschke, B. V. Lotsch, Dark photocatalysis: storage of solar energy in carbon nitride for time-delayed hydrogen generation, *Angew. Chem. Int. Ed.* 56 (2017) 510–514.
- [4] H. Kasap, C.A. Caputo, B.C. Martindale, R. Godin, V.W. Lau, B.V. Lotsch, J. R. Durrant, E. Reisner, Solar-driven reduction of aqueous protons coupled to selective alcohol oxidation with a carbon nitride-molecular Ni catalyst system, *J. Am. Chem. Soc.* 138 (2016) 9183–9192.
- [5] H. Schlömer, J. Kroger, G. Savasci, M.W. Terban, S. Bette, I. Moudrakovski, V. Duppel, F. Podjaski, R. Siegel, J. Senker, R.E. Dinnebier, C. Ochsenfeld, B. V. Lotsch, Structural insights into poly(heptazine imides): a light-storing carbon nitride material for dark photocatalysis, *Chem. Mater.* 31 (2019) 7478–7486.
- [6] Z. Zeng, X. Quan, H. Yu, S. Chen, Y. Zhang, H. Zhao, S. Zhang, Carbon nitride with electron storage property: enhanced exciton dissociation for high-efficient photocatalysis, *Appl. Catal. B Environ.* 236 (2018) 99–106.
- [7] F. Podjaski, J. Kroger, B.V. Lotsch, Toward an aqueous solar battery: direct electrochemical storage of solar energy in carbon nitrides, *Adv. Mater.* 30 (2018) 1705477–1705486.
- [8] S. Amthor, S. Knoll, M. Heiland, L. Zedler, C. Li, D. Nauroozi, W. Tobiaschus, A. K. Mengele, M. Anjass, U.S. Schubert, B. Dietzek-Ivansic, S. Rau, C. Streb, A photosensitizer-polyoxometalate dyad that enables the decoupling of light and dark reactions for delayed on-demand solar hydrogen production, *Nat. Chem.* 14 (2022) 321–327.
- [9] F. Podjaski, B.V. Lotsch, Optoelectronics meets optoelectronics: light storing carbon nitrides and beyond, *Adv. Energy Mater.* 11 (2020) 2003049–2003058.
- [10] P.M. Stanley, F. Sixt, J. Worman, Decoupled solar energy storage and dark photocatalysis in a 3D metal-organic framework, *Adv. Mater.* 35 (2023) 2207280–2207289.
- [11] T. Cai, Y. Liu, L. Wang, W. Dong, G. Zeng, Recent advances in round-the-clock photocatalytic system: mechanisms, characterization techniques and applications, *J. Photochem. Photobiol.* 39 (2019) 58–75.
- [12] G. Zhang, G. Li, T. Heil, S. Zafeirotos, F. Lai, A. Savateev, M. Antonietti, X. Wang, Tailoring the grain boundary chemistry of polymeric carbon nitride for enhanced solar hydrogen production and CO₂ reduction, *Angew. Chem. Int. Ed.* 58 (2019) 3433–3437.
- [13] L. Luo, S. Wang, H. Wang, C. Tian, B. Jiang, Molten-salt technology application for the synthesis of photocatalytic materials, *Energy Technol.* 9 (2021) 2000945–2000959.
- [14] Y. Guo, S. Huang, Y. Guo, Z. Ye, J. Nan, Q. Zhou, Y. Zhu, Efficient degradation of organic pollutants by enhanced interfacial internal electric field induced via various crystallinity carbon nitride homojunction, *Appl. Catal. B Environ.* 312 (2022) 121388–121398.

- [15] Y. Markushyna, P. Lamagni, C. Teutloff, J. Catalano, N. Lock, G. Zhang, M. Antonietti, A. Savateev, Green radicals of potassium poly(heptazine imide) using light and benzylamine, *J. Mater. Chem. A* 7 (2019) 24771–24775.
- [16] D. Tian, H. Yin, L. Liu, B. Li, J. Li, Z. Lou, Plasmonic carbon nitride polymers to boost hydrogen generation, *Adv. Sustain. Syst.* 6 (2022) 2200045–2200054.
- [17] H. Cheng, W. Sun, Y. Lu, H. Li, W. Su, J. Zhang, T. Guo, F. Li, P.S. Francis, Y. Zheng, Hot electrons in carbon nitride with ultralong lifetime and their application in reversible dynamic color displays, *Cell Rep. Phys. Sci.* 2 (2021) 100516–100531.
- [18] Y. Zhang, S. He, W. Guo, Y. Hu, J. Huang, J.R. Mulcahy, W.D. Wei, Surface-plasmon-driven hot electron photochemistry, *Chem. Rev.* 118 (2018) 2927–2954.
- [19] Y. Pan, J. Wang, S. Chen, W. Yang, C. Ding, A. Waseem, H.L. Jiang, Linker engineering in metal-organic frameworks for dark photocatalysis, *Chem. Sci.* 13 (2022) 6696–6703.
- [20] G. Zhang, G. Li, Z.A. Lan, L. Lin, A. Savateev, T. Heil, S. Zafeirotas, X. Wang, M. Antonietti, Optimizing optical absorption, exciton dissociation, and charge transfer of a polymeric carbon nitride with ultrahigh solar hydrogen production activity, *Angew. Chem. Int. Ed.* 56 (2017) 13445–13449.
- [21] L. Lin, Z. Lin, J. Zhang, X. Cai, W. Lin, Z. Yu, X. Wang, Molecular-level insights on the reactive facet of carbon nitride single crystals photocatalysing overall water splitting, *Nat. Catal.* 3 (2020) 649–655.
- [22] L. Huang, Z. Hu, H. Jin, J. Wu, K. Liu, Z. Xu, J. Wan, H. Zhou, J. Duan, B. Hu, J. Zhou, Salt-assisted synthesis of 2D materials, *Adv. Funct. Mater.* 30 (2020) 1908486–1908513.
- [23] Y. Xu, C. Qiu, X. Fan, Y. Xiao, G. Zhang, K. Yu, H. Ju, X. Ling, Y. Zhu, C. Su, K⁺-induced crystallization of polymeric carbon nitride to boost its photocatalytic activity for H₂ evolution and hydrogenation of alkenes, *Appl. Catal. B Environ.* 268 (2020) 118457–118464.
- [24] D. Zhang, X. Han, T. Dong, X. Guo, C. Song, Z. Zhao, Promoting effect of cyano groups attached on g-C₃N₄ nanosheets towards molecular oxygen activation for visible light-driven aerobic coupling of amines to imines, *J. Catal.* 366 (2018) 237–244.
- [25] X. Liu, N. Fechner, M. Antonietti, Salt melt synthesis of ceramics, semiconductors and carbon nanostructures, *Chem. Soc. Rev.* 42 (2013) 8237–8265.
- [26] H. Yu, R. Shi, Y. Zhao, T. Bian, Y. Zhao, C. Zhou, G.L.N. Waterhouse, L.Z. Wu, C. H. Tung, T. Zhang, Alkali-assisted synthesis of nitrogen deficient graphitic carbon nitride with tunable band structures for efficient visible-light-driven hydrogen evolution, *Adv. Mater.* 29 (2017) 1605148–1605155.
- [27] V.W. Lau, I. Moudrakovski, T. Botari, S. Weinberger, M.B. Mesch, V. Duppel, J. Senker, V. Blum, B.V. Lotsch, Rational design of carbon nitride photocatalysts by identification of cyanamide defects as catalytically relevant sites, *Nat. Commun.* 7 (2016) 12165–12175.
- [28] W. Wang, Z. Shu, Z. Liao, J. Zhou, D. Meng, T. Li, Z. Zhao, L. Xu, Sustainable one-step synthesis of nanostructured potassium poly(heptazine imide) for highly boosted photocatalytic hydrogen evolution, *Chem. Eng. J.* 424 (2021) 130332–130342.
- [29] Q. Liu, H. Cheng, T. Chen, T.W.B. Lo, Z. Xiang, F. Wang, Regulating the *OCCHO intermediate pathway towards highly selective photocatalytic CO₂ reduction to CH₃CHO over locally crystallized carbon nitride, *Energy Environ. Sci.* 15 (2022) 225–233.
- [30] D. Zhao, C.L. Dong, B. Wang, C. Chen, Y.C. Huang, Z. Diao, S. Li, L. Guo, S. Shen, Synergy of dopants and defects in graphitic carbon nitride with exceptionally modulated band structures for efficient photocatalytic oxygen evolution, *Adv. Mater.* 31 (2019) 1903545–1903555.
- [31] G. Dong, W. Ho, C. Wang, Selective photocatalytic N₂ fixation dependent on g-C₃N₄ induced by nitrogen vacancies, *J. Mater. Chem. A* 3 (2015) 23435–23441.
- [32] H. Ou, L. Lin, Y. Zheng, P. Yang, Y. Fang, X. Wang, Tri-s-triazine-based crystalline carbon nitride nanosheets for an improved hydrogen evolution, *Adv. Mater.* 29 (2017) 1700008–1700014.
- [33] W. Ren, J. Cheng, H. Ou, C. Huang, M.M. Titirici, X. Wang, Enhancing visible-light hydrogen evolution performance of crystalline carbon nitride by defect engineering, *ChemSusChem* 12 (2019) 3257–3262.
- [34] K.S. Lakhi, D.H. Park, K. Al-Bahily, W. Cha, B. Viswanathan, J.H. Choy, A. Vinu, Mesoporous carbon nitrides: synthesis, functionalization, and applications, *Chem. Soc. Rev.* 46 (2017) 72–101.
- [35] S. An, G. Zhang, K. Li, Z. Huang, X. Wang, Y. Guo, J. Hou, C. Song, X. Guo, Self-supporting 3D carbon nitride with tunable n → pi* electronic transition for enhanced solar hydrogen production, *Adv. Mater.* 33 (2021) 2104361–2104370.
- [36] A.B. Jorge, D.J. Martin, M.T.S. Dhanoa, A.S. Rahman, N. Makwana, J. Tang, A. Sella, F. Corà, S. Firth, J.A. Darr, P.F. McMillan, H₂ and O₂ evolution from water half-splitting reactions by graphitic carbon nitride materials, *J. Phys. Chem. C* 117 (2013) 7178–7185.
- [37] Y. Chen, B. Wang, S. Lin, Y. Zhang, X. Wang, Activation of n → pi* transitions in two-dimensional conjugated polymers for visible light photocatalysis, *J. Phys. Chem. C* 118 (2014) 29981–29989.
- [38] H. Wang, F. Wang, T. Xu, H. Xia, R. Xie, X. Zhou, X. Ge, W. Liu, Y. Zhu, L. Sun, J. Guo, J. Ye, M. Zubair, M. Luo, C. Yu, D. Sun, T. Li, Q. Zhuang, L. Fu, W. Hu, W. Lu, Slowing hot-electron relaxation in mix-phase nanowires for hot-carrier photovoltaics, *Nano Lett.* 21 (2021) 7761–7768.
- [39] H. Ou, C. Tang, X. Chen, M. Zhou, X. Wang, Solvated electrons for photochemistry syntheses using conjugated carbon nitride polymers, *ACS Catal.* 9 (2019) 2949–2955.
- [40] I. Krivtsov, M. Ilkaeva, E.I. García-López, G. Marci, L. Palmisano, E. Bartashevich, E. Grigoreva, K. Matveeva, E. Díaz, S. Ordóñez, Effect of substituents on partial photocatalytic oxidation of aromatic alcohols assisted by polymeric C₃N₄, *ChemCatChem* 11 (2019) 2713–2724.
- [41] L. Jiao, D. Zhang, Z. Hao, F. Yu, X.-J. Lv, Modulating the energy band to inhibit the over-oxidation for highly selective anisaldehyde production coupled with robust h₂ evolution from water splitting, *ACS Catal.* 11 (2021) 8727–8735.
- [42] B. Wu, L. Zhang, B. Jiang, Q. Li, C. Tian, Y. Xie, W. Li, H. Fu, Ultrathin porous carbon nitride bundles with an adjustable energy band structure toward simultaneous solar photocatalytic water splitting and selective phenylcarbinol oxidation, *Angew. Chem. Int. Ed.* 60 (2021) 4815–4822.
- [43] P. Xie, J. Ding, Z. Yao, T. Pu, P. Zhang, Z. Huang, C. Wang, J. Zhang, N. Zecher-Freeman, H. Zong, D. Yuan, S. Deng, R. Shahbazian-Yassar, C. Wang, Oxo dicopper anchored on carbon nitride for selective oxidation of methane, *Nat. Commun.* 13 (2022) 1375–1385.
- [44] D. Zhang, P. Ren, W. Liu, Y. Li, S. Salli, F. Han, W. Qiao, Y. Liu, Y. Fan, Y. Cui, Y. Shen, E. Richards, X. Wen, M.H. Rummeli, Y. Li, F. Besenbacher, H. Niemantsverdriet, T. Lim, R. Su, Photocatalytic abstraction of hydrogen atoms from water using hydroxylated graphitic carbon nitride for hydrogenative coupling reactions, *Angew. Chem. Int. Ed.* 61 (2022) e202204256–e202204265.
- [45] H. Ji, F. Chang, X. Hu, W. Qin, J. Shen, Photocatalytic degradation of 2,4,6-trichlorophenol over g-C₃N₄ under visible light irradiation, *Chem. Eng. J.* 218 (2013) 183–190.
- [46] Y. Shiraishi, S. Kanazawa, Y. Sugano, D. Tsukamoto, H. Sakamoto, S. Ichikawa, T. Hirai, Highly selective production of hydrogen peroxide on graphitic carbon nitride (g-C₃N₄) photocatalyst activated by visible light, *ACS Catal.* 4 (2014) 774–780.
- [47] F. Su, S.C. Mathew, G. Lipner, X. Fu, M. Antonietti, S. Blechert, X. Wang, Mpg-C₃N₄-catalyzed selective oxidation of alcohols using O₂ and visible light, *J. Am. Chem. Soc.* 132 (2010) 16299–16301.
- [48] S. Samanta, S. Khilari, D. Pradhan, R. Srivastava, An efficient, visible light driven, selective oxidation of aromatic alcohols and amines with O₂ using BiVO₄/g-C₃N₄ nanocomposite: a systematic and comprehensive study toward the development of a photocatalytic process, *ACS Sustain. Chem. Eng.* 5 (2017) 2562–2577.
- [49] X. Bao, M. Liu, Z. Wang, D. Dai, P. Wang, H. Cheng, Y. Liu, Z. Zheng, Y. Dai, B. Huang, Photocatalytic selective oxidation of HMF coupled with H₂ evolution on flexible ultrathin g-C₃N₄ nanosheets with enhanced N–H interaction, *ACS Catal.* 12 (2022) 1919–1929.
- [50] J. Ding, W. Xu, H. Wan, D. Yuan, C. Chen, L. Wang, G. Guan, W.-L. Dai, Nitrogen vacancy engineered graphitic C₃N₄-based polymers for photocatalytic oxidation of aromatic alcohols to aldehydes, *Appl. Catal. B Environ.* 221 (2018) 626–634.
- [51] B. Long, Z. Ding, X. Wang, Carbon nitride for the selective oxidation of aromatic alcohols in water under visible light, *ChemSusChem* 6 (2013) 2074–2078.
- [52] M.J. Lima, P.B. Tavares, A.M.T. Silva, C.G. Silva, J.L. Faria, Selective photocatalytic oxidation of benzyl alcohol to benzaldehyde by using metal-loaded g-C₃N₄ photocatalysts, *Catal. Today* 287 (2017) 70–77.
- [53] Z. Xu, Y. Li, Y. Cao, R. Du, Z. Bao, S. Zhang, F. Shao, W. Ji, J. Yang, G. Zhuang, S. Deng, Z. Wei, Z. Yao, X. Zhong, J. Wang, Trace water triggers high-efficiency photocatalytic hydrogen peroxide production, *J. Energy Chem.* 64 (2022) 47–54.
- [54] E.I. García-López, Z. Abbasi, F. Di Franco, M. Santamaria, G. Marci, L. Palmisano, Selective oxidation of aromatic alcohols in the presence of C₃N₄ photocatalysts derived from the polycondensation of melamine, cyanuric and barbituric acids, *Res. Chem. Intermed.* 47 (2021) 131–156.
- [55] Q. Yang, T. Wang, F. Han, Z. Zheng, B. Xing, B. Li, Bimetal-modified g-C₃N₄ photocatalyst for promoting hydrogen production coupled with selective oxidation of biomass derivative, *J. Alloy. Compd.* 897 (2022) 163177–163187.
- [56] G. Marci, E.I. García-López, L. Palmisano, Polymeric carbon nitride (C₃N₄) as heterogeneous photocatalyst for selective oxidation of alcohols to aldehydes, *Catal. Today* 315 (2018) 126–137.
- [57] L. Luo, Z.-j. Wang, X. Xiang, D. Yan, J. Ye, Selective activation of benzyl alcohol coupled with photoelectrochemical water oxidation via a radical relay strategy, *ACS Catal.* 10 (2020) 4906–4913.
- [58] Q. Zhang, Y.-C. Chu, Z. Liu, M. Hong, W. Fang, X.-P. Wu, X.-Q. Gong, Z. Chen, Construction of triazine-heptazine-based carbon nitride heterojunctions boosts the selective photocatalytic C–C bond cleavage of lignin models, *Appl. Catal. B Environ.* 331 (2023) 122688–122701.
- [59] L. Chen, D. Zhu, J. Li, X. Wang, J. Zhu, P.S. Francis, Y. Zheng, Sulfur and potassium co-doped graphitic carbon nitride for highly enhanced photocatalytic hydrogen evolution, *Appl. Catal. B Environ.* 273 (2020) 119050–119059.
- [60] X.L. Wang, W.Q. Fang, W. Liu, Y. Jia, D. Jing, Y. Wang, L.-Y. Yang, X.-Q. Gong, Y.-F. Yao, H.G. Yang, X. Yao, Brønsted base site engineering of graphitic carbon nitride for enhanced photocatalytic activity, *J. Mater. Chem. A* 5 (2017) 19227–19236.
- [61] S. Guo, Z. Deng, M. Li, B. Jiang, C. Tian, Q. Pan, H. Fu, Phosphorus-doped carbon nitride tubes with a layered micro-nanostructure for enhanced visible-light photocatalytic hydrogen evolution, *Angew. Chem. Int. Ed.* 55 (2016) 1830–1834.